Journal of Computational Physics 228 (2009) 1521–1540

Contents lists available at ScienceDirect

Journal of Computational Physics

journal homepage: www.elsevier.com/locate/jcp

Phase field modeling of liquid jets in low gravity

David J. Chato *

NASA Glenn Research Center, 21000 Brookpark Rd., Mail Stop 301-3, Cleveland, OH 44135, United States

ARTICLE INFO

Article history:
Received 31 July 2006
Received in revised form 22 June 2007
Accepted 29 October 2008
Available online 7 November 2008

Keywords:
Incompressible flow
Surface tension
Low gravity
Liquid jets

ABSTRACT

An axisymmetric phase field model is developed and used to model surface tension forces on liquid jets in microgravity. The previous work in this area is reviewed and a baseline drop tower experiment selected for model comparison. The model is solved numerically with a compact fourth order stencil on an equally spaced axisymmetric grid. After grid convergence studies, a grid is selected and all drop tower tests modeled. Agreement was assessed by comparing predicted and measured free surface rise. Trend wise agreement is good but agreement in magnitude is only fair. Suspected sources of disagreement are the simple turbulence model and the existence of slosh baffles in the experiment that were not included in the model. Parametric investigation was conducted to study the influence of key parameters on the geysers formed by jets in microgravity. Investigation of the contact angle showed the expected trend of increasing contact angle increasing geyser height. Investigation of the tank radius showed some interesting effects and demonstrated the zone of free surface deformation is quite large. Variation of the surface tension with a laminar jet showed clearly the evolution of free surface shape with Weber number. A breakthrough Weber number of 1 was predicted by the variation of the surface tension model which is close to the experimentally measured Weber number of 1.5 found in prior experimental work.

Published by Elsevier Inc.

1. Introduction

Microgravity poses many challenges to the designer of fluid storage for spacecraft. Chief among these are the lack of phase separation in the fluid and the need to supply vapor-free liquid or liquid-free vapor to the required spacecraft processes. One of the principal causes of lack of phase separation is the creation of liquid jets. A jet can be created by liquid filling, settling of the fluid to one end of the tank, or even closing a valve to stop the liquid outflow. In normal gravity the gravitational force controls and restricts the liquid jet flow, but in microgravity jets must be contained by surface tension forces. Recent NASA experiments in microgravity [1–6] have brought a wealth of data of jet behavior in microgravity. The Vented Tank Resupply Experiment [6] was surprising in that although it contained a complex geometry of baffles and vanes the limit on liquid inflow was the emergence of a liquid jet from the top of the vane structure. Clearly understanding the restraint of liquid jets by surface tension is key to managing fluids in low gravity.

Flow of a submerged axial jet constrained by surface tension in low gravity is similar to stagnation flow against a plate in that the jet hits the constraining surface and is deflected radially out. However, in low gravity the ability of the constraining surface to move in response to the exerted force is unique. In fact to increase the restraining force on the jet as flow rate increases, the surface must deform to decrease the radius of curvature of the free surface, thereby increasing the surface tension force. Eventually the limit is reached where the radius curvature required is sufficiently smaller than the jet diameter

* Tel.: +1 216 977 7488; fax: +1 216 977 7545.
E-mail address: David.J.Chato@nasa.gov

0021-9991/$ - see front matter Published by Elsevier Inc.
doi:10.1016/j.jcp.2008.10.031

Nomenclature

a	height
C	phase distribution
d	jet diameter
D	tank diameter
f	free energy
g	wall function
k	equation exponent
L	tank length
M	radial correction factor
P	pressure
r	jet radius
Re	Reynolds number = $\frac{\rho u_{av} d}{\mu}$
u	velocity
u_{av}	average jet velocity
V	volume
We	Weber number = $\frac{\rho u_{av}^2 r}{2\sigma}$
x	radial distance
y	axial distance
α	constant 1
β	constant 2
θ_c	contact angle
κ	constant 3
ρ	density
σ	surface tension
ϕ	potential function
Ψ	barrier function

such that it can no longer restrain the jet. When the deformation of the free surface is large the restraining bulge is long and slender. At this point several other mechanisms act to break down the jet, such as columnar buckling or the Taylor instability where surface waves grow to such amplitude that they pinch a droplet off from the jet.

To model this low gravity phenomenon a numerical method that tracks the fluid motion and the surface tension forces is required. Jacqmin [7] has developed a phase field model that converts the delta-function surface tension force into a continuum function that peaks at the free surface and decays rapidly away. Previous attempts at this formulation have been criticized for smearing the interface but by sharpening the phase function, double gridding the fluid function and using a higher order solution for the fluid function these concerns have been ameliorated. Although Jacqmin laid out the basic axisymmetric scheme the computer code and all the examples in the paper are planar. This paper extends the work of Jacqmin by adapting his code solve to axisymmetric problems, formulating boundary conditions for both the axisymmetric centerline and wall boundaries including contact angle, and then solving for the axial jet flow.

2. Review of literature

NASA Drop Tower Data is found in Refs. [8–18]. Symons [8–11] and Spuckler [12] studied the liquid inflow via axial jet into a broad range of tank shapes both empty and partially full. Symons' work establishes an empirical limit for jets of Weber number (We) equal to 1.3–1.5 depending on jet velocity profile, where

$$We = \frac{\rho u_{av}^2 r}{2\sigma}. \tag{1}$$

Staskus [13] extends the work of Symons by placing baffles in front of the jet. However, no attempt is made to analyze these complex flows. Instead results are reported as a ratio of improvement to the unbaffled jet Weber number. Labus et al. [14] also studies the effect of baffles including ones that break the central jet into several small jets. Aydelott [15–17] looks at the problem of a recirculating jet where the liquid level is held constant. Results are classified into four flow patterns, dissipation, geyser formation, aft collection, and circulation. It is the geyser formation/aft collection we concern ourselves with in this paper. Aydelott's assessment that a drop in mixing accompanies this transition indicates the transition's importance. Labus [18] studies both stagnation flow and free surface shape, but is concerned with the free surface of the back side of a liquid jet stagnated against a flat plate in microgravity.

Shuttle based experiments in Refs. [1–6] provide valuable low gravity data. Video of Plexiglas tanks during shuttle orbital flight provide several improvements over drop tower tests; including increasing the scale from 4 in. tanks to 12 in. tanks and extending the duration of test from 5 s to half-an-hour. Tank Pressure Control Experiment has flown three times. The first

flight focused on the mixing studies of Aydelott. Advances over Aydelott included actual heat transfer data by using a condensing fluid (refrigerant 113) and longer duration. Bentz [1–3] was able to confirm the geysering and circulating regimes of Aydelott, but encountered an asymmetric regime between the two that was even lower heat transfer than aft collection, the lowest mixing regime of Aydelott. The second flight of TPCE focused mostly on rapid boiling phenomena, but contains some further tests on mixing. Hasan [4] confirms the findings of Bentz. The third flight [5] was done at a lower fill level but confirms the results of the other flights. The Vented Tank Resupply Experiment [6] was designed to look at vanes rather than axial jets, but as noted previously exhibits the classic geysering behavior.

Analytical work is listed in Refs. [7,19–29]. Concus [19,20] provides differential equations of the free surface problem, but analyzes only static cases. Nickell et al. [21] analyzes flow from a jet into a liquid and the resultant free surface shape for a normal gravity application, but removes all surface tension from the analysis as secondary. Hochstein [22,23] analyzes the microgravity mixing with a volume of fluid approach, but uses only a limited approximation to model the surface tension. Aydelott et al. [24] and Der and Stevens [25] both analyze the motion of a bubble in the oxygen tank during separation of a Centaur stage with VOF models; noteworthy in these is again the appearance of a geyser. Tegart [26] shows the application of the surface Evolver code of Brakke [27] to actual tank shapes. Brackbill et al. [28] develops an improved surface tension model for VOF codes, but only shows one example of its use for axial jets. Schrader and Hochstein [29] uses a Runga–Kutta scheme to solve the differential equation of free surface deformation in response to an imposed pressure field. This approach is quite promising but does not always converge and limits the interaction between the flow field and the free surface. Jacqmin [7] developed a phase field model of surface tension and implemented as a fourth order accurate scheme using a compact 9-point stencil. Although Jacqmin lays out the basic axisymmetric scheme the computer code and all the examples in his paper are planar. The Jacqmin model will serve as the basis for the present analysis.

3. Model

3.1. Introduction

To model the fluid motion the Navier–Stokes equations are formulated for low-speed incompressible flow. This paper will document the adaptation of the Jacqmin algorithm to the problem of restraint of liquid jets. Velocity and pressure are placed on a staggered grid, with velocity being tracked at cell faces and pressure at cell centers. To track the free surface a color function is introduced which tracks liquid as 1/2 and gas as $-1/2$. Enhancements to the Jacqmin model include formulation of an axisymmetric fourth order model, implementation of a symmetric boundary condition at the tank centerline, and extension of the wall wetting boundary condition to fourth order accuracy. A simple velocity forcing function has been added to simulate the jet without violating continuity.

3.2. Phase model of surface tension

Surface tension can be expressed as a free energy field. The expression for this energy in our formulation is given by

$$f = \frac{1}{2}\alpha|\nabla C|^2 + \beta\Psi(C), \tag{2}$$

where C is a phase distribution function and Ψ is a barrier function that is maximum at the interface and dies away as the phase becomes uniform. This formulation is extracted from Van der Waals [30] and inherently implies that the equilibrium free surface position is the one where the free energy is minimized. In order to model this behavior the physical Ψ that dies away on the molecular scale is approximated by a function with similar behavior on a larger scale such as

$$\Psi(C) = \frac{2^{2k}}{2k+2}C^{2k+2} - \frac{1}{2}C^2 + \frac{2k}{8(2k+2)}. \tag{3}$$

This function has the required properties of being maximum at $C = 0$ and dying away to 0 at both 1/2 and $-1/2$. If we define our C function as being 1/2 when the phase is liquid and $-1/2$ when the phase is gas this will produce the required behavior. Higher values of k produce sharper peaks. For our solution we will choose $k = 16$. This was a value determined by test runs to produce a sharp peak without requiring excessive iterations to solve.

To study the transients of the free surface some additional formulations are required. We define a potential function as the rate of change in f per unit volume with respect to C

$$\phi = \frac{\delta \int f\,dV}{\delta C} = \beta\Psi'(C) - \alpha\nabla^2 C. \tag{4}$$

To determine the relation between α and β we look at the relation of a dividing surface between two infinite reservoirs one of gas and one of liquid. Although the surface tension force is zero, the surface tension itself is given by the difference between the thermodynamic energy of each phase. This is given by our model as

$$\sigma = \alpha\int_{-\infty}^{+\infty}\left(\frac{dC}{dx}\right)^2 dx. \tag{5}$$

Since the system is in equilibrium the ϕ is zero so

$$\beta\Psi'(C) - \alpha\nabla^2 C = \beta\frac{d\Psi}{dC}(C) - \alpha\frac{d^2C}{dx^2} = 0. \tag{6}$$

Approximating the solution numerically yields

$$\sigma = .371517\sqrt{\alpha\beta}. \tag{7}$$

$\alpha$is adjusted until the interface just spans 3 velocity grid points (5 color function grid points). On a grid of 75 × 300 for a 5 cm by 20 cm computational region and a σ = 22.4 dynes/cm, an α of 5.1139 was used. This is the grid resolution used for the majority of calculations used in this dissertation. Other grid resolutions use an α scaled from this value by the change in grid size.

For the phase field interface to move freely through the grid diffusion of the C function is required. Again we use as a model for our macro-scale model equations developed for the molecular scale. Cahn and Hillard [31] approximate the transients of the free surface by setting the diffusion fluxes as proportional to the potential gradient. In equation form this is

$$\frac{\partial C}{\partial t} = \kappa\nabla^2\phi. \tag{8}$$

In the microscale equation of Hillard and Cahn kappa is matched to molecular properties. In our macro-scale formulation it is a somewhat arbitrary constant. There are constraints however. If too small a value of is used, then the interface becomes too thick in some places and too thin in others producing unrealistic solutions. If too large a value of is used spurious secondary flows will be generated in the bulk fluid. For the calculations of this paper kappa of 0.00021112 was used. This gives us two coupled Poisson equations to solve for the phase distribution. To add the effects of fluid motion we must use the Navier–Stokes equations. The continuity equation for incompressible flow is

$$\vec{\nabla}\bullet\vec{u} = 0. \tag{9}$$

The momentum equations for each direction are given by

$$\rho\frac{Du_i}{Dt} = \rho\frac{\partial u_i}{\partial t} + \rho\sum_j u_j\frac{\partial u_i}{\partial x_j} = -\vec{\nabla}P + \mu\nabla^2 u_i - C\vec{\nabla}\phi. \tag{10}$$

3.3. Fourth order formulation of the governing equations

The equations of the previous section cannot be solved directly but must be solved numerically. To keep the interface as sharp as possible a compact fourth order stencil is used. The equation

$$\nabla^2 u = f \tag{11}$$

was show by Collatz [32] to be approximated by

$$\left[\nabla^2 + \frac{1}{12}(\Delta x)^2\nabla^4\right]u = f + \frac{1}{12}\nabla^2 f + O(\Delta x^4). \tag{12}$$

Using central differencing on a square Cartesian grid one obtains the following computational stencil:

$$\frac{1}{6}\begin{bmatrix}1 & 4 & 1\\ 4 & -20 & 4\\ 1 & 4 & 1\end{bmatrix}u = \frac{(\Delta x)^2}{12}\begin{bmatrix}0 & 1 & 0\\ 1 & 8 & 1\\ 0 & 1 & 0\end{bmatrix}f + O(\Delta x^4). \tag{13}$$

With some slight modification (We retain the $\nabla^2\phi$ term because it is calculated by Eq. (8) and correct our stencil for radial expansion) we can use this to rewrite the potential equation (4) as

$$\frac{\alpha}{6(\Delta x)^2}\begin{bmatrix}M_- & 4 & M_+\\ 4M_- & -20 & 4M_+\\ M_- & 4 & M_+\end{bmatrix}C = \frac{\beta}{12}\begin{bmatrix}0 & 1 & 0\\ M_- & 8 & M_+\\ 0 & 1 & 0\end{bmatrix}\Psi'(C) - \begin{bmatrix}0 & 0 & 0\\ 0 & 1 & 0\\ 0 & 0 & 0\end{bmatrix}\phi + \frac{(\Delta x)^2}{12}\nabla^2\phi + O(\Delta x^4), \tag{14}$$

where

$$M_\pm = (x_\pm + x_0)/2x_0. \tag{15}$$

3.3.1. Symmetry boundary

At the centerline (r = 0) the problem is symmetric therefore along this edge the equation becomes

$$\frac{\alpha}{6(\Delta x)^2}\begin{bmatrix}2 & 4\\ -28 & 16\\ 2 & 4\end{bmatrix}C = \frac{\beta}{12}\begin{bmatrix}1 & 0\\ 6 & 4\\ 1 & 0\end{bmatrix}\Psi'(C) - \begin{bmatrix}0 & 0\\ 1 & 0\\ 0 & 0\end{bmatrix}\phi - \frac{(\Delta x)^2}{12}\nabla^2\phi + O(\Delta x^4). \tag{16}$$

3.3.2. Wall boundary

At the outer wall two boundary conditions will be used. First is the no flux boundary

$$\frac{\partial \phi}{\partial x} = 0. \tag{17}$$

The second is a bit more complicated. Postulating a wall energy function of the form

$$F_w = \int \sigma g(C) dA, \tag{18}$$

where g is a function chosen to yield the correct contact angle. Then the diffusively controlled equilibrium at the wall is

$$\alpha \frac{\partial C}{\partial r} + \sigma g'(C) = 0 \tag{19}$$

for our purposes

$$g(C) = \cos(\theta_c)[6C^2 - 1.5]. \tag{20}$$

Substituting into our main equation

$$\frac{\alpha}{6(\Delta x)^2}\begin{bmatrix} 2 & 4 \\ 8 - 4\frac{\Delta x}{r} & -20 + 4\frac{\Delta x}{r} \\ 2 & 4 \end{bmatrix} C = \frac{\beta}{12}\begin{bmatrix} 0 & 1 \\ 2 & 8 \\ 0 & 1 \end{bmatrix} \Psi'(C) - \begin{bmatrix} 0 & 0 \\ 1 & 0 \\ 0 & 0 \end{bmatrix} \phi - \frac{(\Delta x)^2}{12}\nabla^2\phi + \left(\frac{2}{\Delta x} + \frac{1}{3r} + \frac{\Delta x}{3r^2}\right) g' + \left(\frac{\Delta x}{6} - \frac{\Delta x^2}{12r}\right) \Psi'' \frac{\beta}{\alpha} g' + O(\Delta x^4). \tag{21}$$

A similar approach is used for the top wall except that for simplicity θ_c is set to 90° resulting in $g = g' = 0$ and the boundary being symmetric. This should not affect the results of the calculation since interface flow along the top wall does not occur in our problem until after free surface penetration. The equation for the top wall is

$$\frac{\alpha}{6(\Delta x)^2}\begin{bmatrix} 4M_- & -20 & 4M_+ \\ 2M_- & 8 & 2M_+ \end{bmatrix} C = \frac{\beta}{12}\begin{bmatrix} M_- & 8 & M_+ \\ 0 & 2 & 0 \end{bmatrix} \Psi'(C) - \begin{bmatrix} 0 & 1 & 0 \\ 0 & 0 & 0 \end{bmatrix} \phi - \frac{(\Delta x)^2}{12}\nabla^2\phi + O(\Delta x^4). \tag{22}$$

The bottom wall is done the same as the top wall. Here the logic used to justify θ_c is set to 90° is that the wall is only in contact with liquid throughout our runs. The equation for the bottom wall is

$$\frac{\alpha}{6(\Delta x)^2}\begin{bmatrix} 2M_- & 8 & 2M_+ \\ 4M_- & -20 & 4M_+ \end{bmatrix} C = \frac{\beta}{12}\begin{bmatrix} 0 & 2 & 0 \\ M_- & 8 & M_+ \end{bmatrix} \Psi'(C) - \begin{bmatrix} 0 & 0 & 0 \\ 0 & 1 & 0 \end{bmatrix} \phi - \frac{(\Delta x)^2}{12}\nabla^2\phi + O(\Delta x^4). \tag{23}$$

3.3.3. Corner boundaries

Equation for the top inner boundary combining the symmetry and top wall boundaries

$$\frac{\alpha}{6(\Delta x)^2}\begin{bmatrix} -28 & 16 \\ 4 & 8 \end{bmatrix} C = \frac{\beta}{12}\begin{bmatrix} 6 & 4 \\ 2 & 0 \end{bmatrix} \Psi'(C) - \begin{bmatrix} 1 & 0 \\ 0 & 0 \end{bmatrix} \phi - \frac{(\Delta x)^2}{12}\nabla^2\phi + O(\Delta x^4). \tag{24}$$

Equation for the bottom inner boundary combing symmetry and bottom wall boundary

$$\frac{\alpha}{6(\Delta x)^2}\begin{bmatrix} 4 & 8 \\ -28 & 16 \end{bmatrix} C = \frac{\beta}{12}\begin{bmatrix} 2 & 0 \\ 6 & 4 \end{bmatrix} \Psi'(C) - \begin{bmatrix} 0 & 0 \\ 1 & 0 \end{bmatrix} \phi - \frac{(\Delta x)^2}{12}\nabla^2\phi + O(\Delta x^4). \tag{25}$$

Equation for the top outer boundary combining top and outer boundary

$$\frac{\alpha}{6(\Delta x)^2}\begin{bmatrix} 8 - 4\frac{\Delta x}{r} & -20 + 4\frac{\Delta x}{r} \\ 4 & 8 \end{bmatrix} C = \frac{\beta}{12}\begin{bmatrix} 2 & 8 \\ 0 & 2 \end{bmatrix} \Psi'(C) - \begin{bmatrix} 0 & 1 \\ 0 & 0 \end{bmatrix} \phi - \frac{(\Delta x)^2}{12}\nabla^2\phi + \left(\frac{2}{\Delta x} + \frac{1}{3r} + \frac{\Delta x}{3r^2}\right) g' + \left(\frac{\Delta x}{6} - \frac{\Delta x^2}{12r}\right) \Psi'' \frac{\beta}{\alpha} g' + O(\Delta x^4). \tag{26}$$

Equation for the bottom outer boundary

$$\frac{\alpha}{6(\Delta x)^2}\begin{bmatrix} 4 & 8 \\ 8 - 4\frac{\Delta x}{r} & -20 + 4\frac{\Delta x}{r} \end{bmatrix} C = \frac{\beta}{12}\begin{bmatrix} 0 & 2 \\ 2 & 8 \end{bmatrix} \Psi'(C) - \begin{bmatrix} 0 & 0 \\ 0 & 1 \end{bmatrix} \phi - \frac{(\Delta x)^2}{12}\nabla^2\phi + \left(\frac{2}{\Delta x} + \frac{1}{3r} + \frac{\Delta x}{3r^2}\right) g' + \left(\frac{\Delta x}{6} - \frac{\Delta x^2}{12r}\right) \Psi'' \frac{\beta}{\alpha} g' + O(\Delta x^4). \tag{27}$$

3.4. Implementation as a CFD code

The previous equations form a complete set of differential equations that can be solved for the fluid transient motion. Each equation is solved sequentially and numeric techniques specific to each equation are used to achieve the desired level of accuracy.

3.4.1. Solution for the potential field

A Newton–Raphson iteration is used to project the body centered values of C to the cell boundaries and produce a ϕ field consistent with Eq. (8).

3.4.2. Advection of phase quantities

Eq. (14) and its boundary equations form a matrix equation that is solved using the current values of C and ϕ to project new values. This process is iterated four times to smooth the solution.

3.4.3. Solution of the velocity field

Eq. (10) is used to predict the change in velocity field. The projected velocity changes are used to calculate viscous stresses that are then used to correct the velocity change.

3.4.4. Solution of the pressure equation

The velocity changes are fed into the pressure Poisson equation that is solved by successive over relaxation to produce a uniform static pressure field consistent with our incompressible flow assumption.

4. Comparison to experiment

4.1. Aydelott's test data

After implementation of the code in axisymmetric form was complete and verified by several test cases, the drop tower runs of Aydelott [17] were modeled. Aydelott looked at the problem of a recirculating jet where the liquid level is held constant. Results are classified into four flow patterns, dissipation, geyser formation, aft collection, and circulation. It is the dissipation/geyser formation we concern ourselves with in this paper. Aydelott's assessment that this transition is accompanied by a drop in mixing indicates the transition's importance. Table 1 shows a compilation of Aydelott's zero-g runs in these regimes. Little of the drop tower film remains, but Fig. 1 shows the time history of run 15 (Re = 450, fill level 50%). Times are estimated from frame counts since the clock is out of focus. Four tanks were used; a 10 cm diameter cylindrical tank with hemispherical ends 20 cm long including the ends (labeled a in Table 1); a similar tank with the end opposite the inlet inverted (labeled b); the same as the second except with ring slosh baffles at the 30% and 77% full levels (labeled c); and a 10 cm sphere. Spherical tank data has been omitted since we cannot model curved boundaries. Results were run with a 0.4 cm diameter inlet of length either 1 cm from the tank bottom or 8 cm from the bottom. The flow rate was varied from 17 to 194 cm/s.

4.2. Approximation of the liquid jet

Since the solution of the Navier–Stokes equation we used conserves mass strongly, injecting liquid into the solution space posses many difficulties. To avoid these problems the entering jet was modeled as a recirculating region where the axial

Table 1
Experimental results of Aydelott in the dissipation and geyser formation regimes.

Test	Tank shape	Liquid fill vol%	Jet Reynolds number	Jet Weber number	Ratio of geyser height to tank diameter
1	c	29	630	0.96	0.55
2	c	29	900	1.09	.80
12	b	39	450	.49	.36
13	b	39	900	1.11	.84
14	b	39	1290	1.59	2.16
15	c	50	450	.39	.42
17	c	51	630	.78	.34
19	c	52	900	.81	.52
24	a	52	1320	1.16	1.45
50	b	60	450	.37	.24
51	b	60	900	.72	.42
52	b	60	1320	1.05	1.10
53	b	73	900	.57	.30
57	b	73	1270	.78	.70
64	b	91	480	.31	.10
65	c	91	900	.48	.20
66	c	92	1290	.62	.48

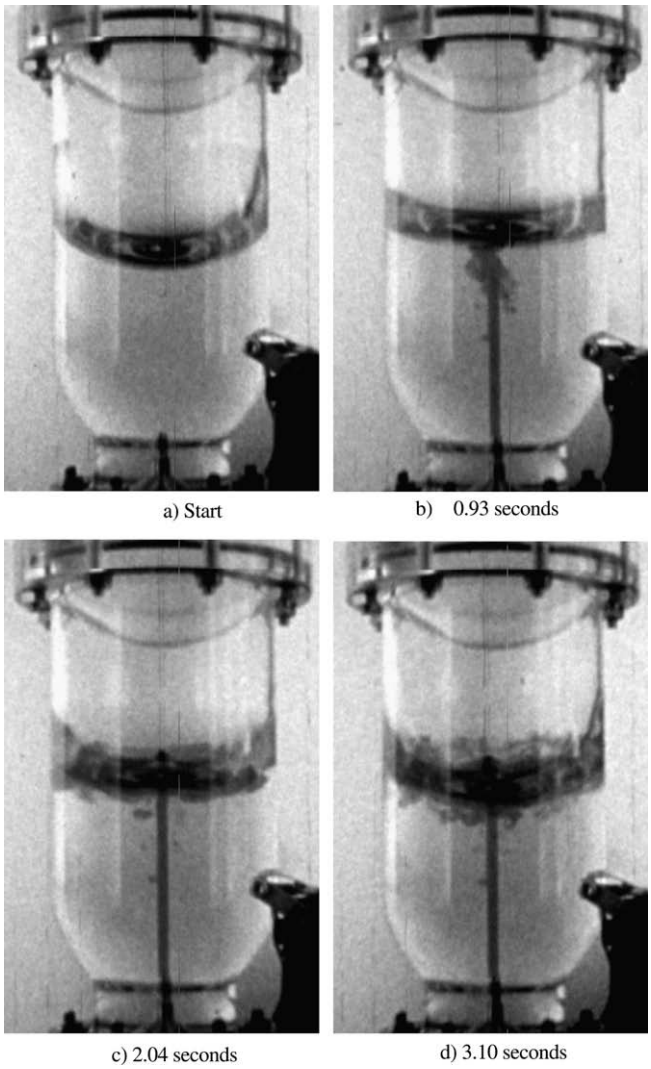

Fig. 1. Drop tower run 15, fill 50%, jet velocity 17 cm/s.

velocity was forced to a desired value. This allowed the radial velocity to entrain liquid into the jet and thus conserve mass. A 0.5 cm length for this region was chosen since this appeared to be long enough so at the top of the region the mass entrainment was sufficient such that the v velocity was the dominant fluid motion.

4.3. Grid sensitivity

A grid sensitivity test was done to confirm the choice of a 75 by 300 grid for modeling. This grid is fine enough to place two points in the starting jet, but yet not overly tax the computer for storage and run time. Comparison to a 100 by 400 grid showed little change in either flow field or free surface shape. Fig. 2 shows the comparison. Note: although the plot time for the finer grid is off by 0.07 s due to differing timesteps, the problem sufficient slow moving that this does not represent a substantial mismatch.

4.4. Computer predictions for laminar runs

Aydelott's test were first modeled using a laminar solution. A number of cases were observed by Aydelott to be either laminar or transitional with Reynolds number between 450 and 1290. Figs. 3 and 4 show representative computer predictions of Aydelott's tests. Fig. 3 is a low flow rate test that only slightly deforms the free surface. Fig. 4 is a high flow rate test where the geyser continues to grow throughout until it eventually contacts the far boundary of the grid. The model handed the free surface deformation quite nicely, even to the point of modeling geyser growth in the regime where the free surface is no longer restrained (see Fig. 4).

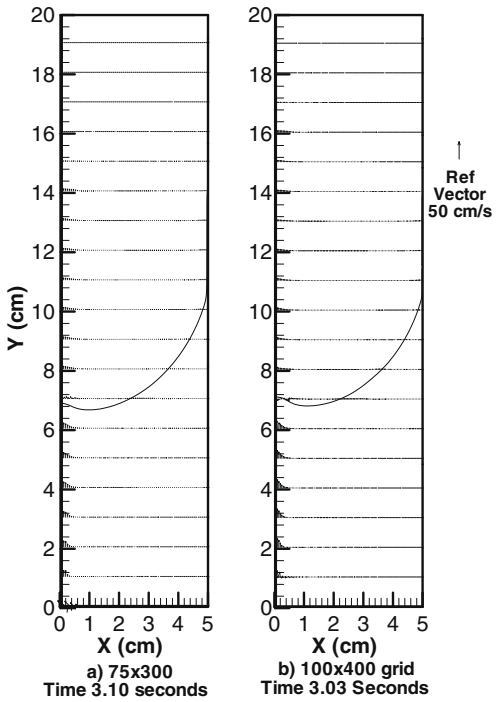

Fig. 2. Comparison between 75 × 300 and 100 × 400, grid resolutions fill 39%, jet velocity 17 cm/s (Reynolds number 450).

4.4.1. On laminarity of the jet inflow

Classic analysis of the liquid-in-liquid jet indicates very low stability. Viilu [33] showed a limit as low as $Re = 11$. McNaughton and Sinclair [34] using a more practical analysis divided the liquid-in-liquid jet into four regimes:

dissipated laminar ($Re < 300$ approx.);
fully laminar jets ($300 < Re < 1000$ approx.);
semi-turbulent ($1000 < Re < 3000$ approx);
fully turbulent ($Re > 3000$).

Their transition numbers are somewhat a function of the length of their apparatus. Dissipated jets only made it a portion of the way across the test chamber before dissipating into the bulk liquid via the same breakdown reported in the previous reference. This distance increased with increasing *Re* number until a laminar jet spanned the length of their test chamber the fully laminar region. As the *Re* increased further a turbulent flow region began to emerge near the far end of the jet. The length of laminar flow would begin to decrease as the flow increased until eventually the jet would become turbulent right at the nozzle marking the transition to the final region.

Their data for the length of the laminar region was given by the correlation

$$a/d = 9.97 \times 10^7 Re^{-2.46} (D/d)^{-0.48} (L/d)^{0.74}. \tag{28}$$

Our runs of *Re* 450, 630 are in the fully laminar region. The *Re* 900 run should transition to turbulence at a distance of 8.3 cm and *Re* 1290 at 3.4 cm. Aydelott reviewing the data reports the following findings. No spreading at *Re* 450, for *Re* 630 no spreading if the liquid height over the jet was less than 2.5 cm; spreading consistent with a laminar jet thereafter. *Re* 900 a jet intermediate between laminar and turbulent. And for $Re > 1500$ a fully turbulent jet.

4.4.2. Visual comparison

Comparison of the data to the model show similarity in jet spread and flow motion. The model even captures the vortex shedding from the tip of the geyser as the flow develops although the axisymmetric nature of the model forces more regularity in the vortex shedding than is seen in the drop tower film.

4.4.3. Predicted geyser height

Model predictions of geyser heights are shown in Table 2. For comparison the measured heights of Aydelott are also shown. Although the model under predicts the experiment for the lowest flow rate it over predicts at the next highest rate. It predicts breakthrough at a flow rate of 34 cm/s even though the experimental data indicate the jet is still contained. The

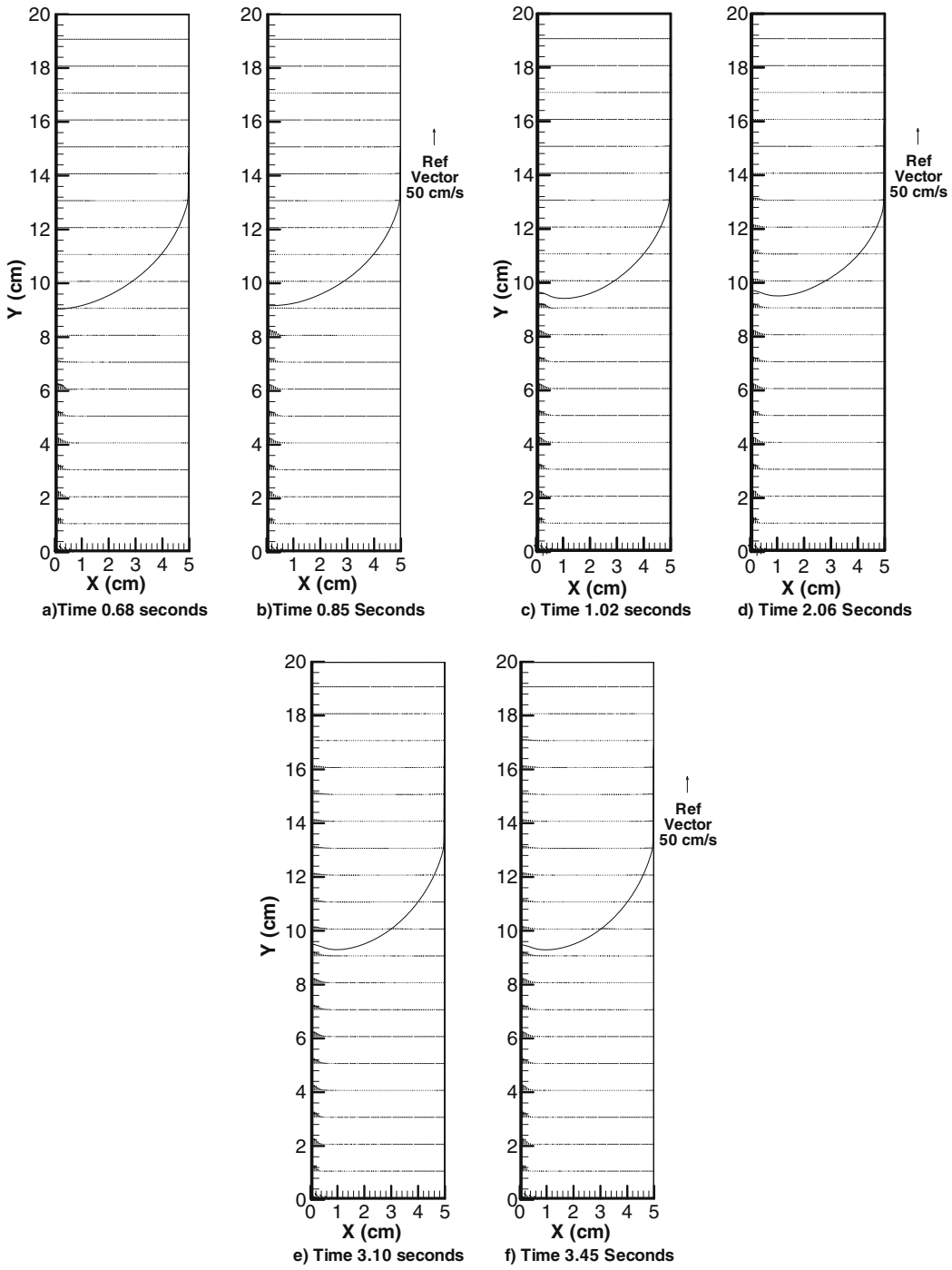

Fig. 3. Test 15, jet velocity 17 cm/s, fill height 9.1 cm at the centerline.

over prediction is believed due to the lack of turbulence modeling. It is well known that turbulent jets spread at a much higher rate than laminar jets. This increased spread will lower the centerline velocity more quickly and increase the area of the jet at the free surface, decreasing the amount of surface deformation required to contain the jet.

4.5. Turbulence modeling

In an effort to improve the prediction at higher Reynolds number flows a simple turbulence model was introduced. Simple mixing length models of turbulence suggest that for the free jet flow can be approximated by using a constant turbulent

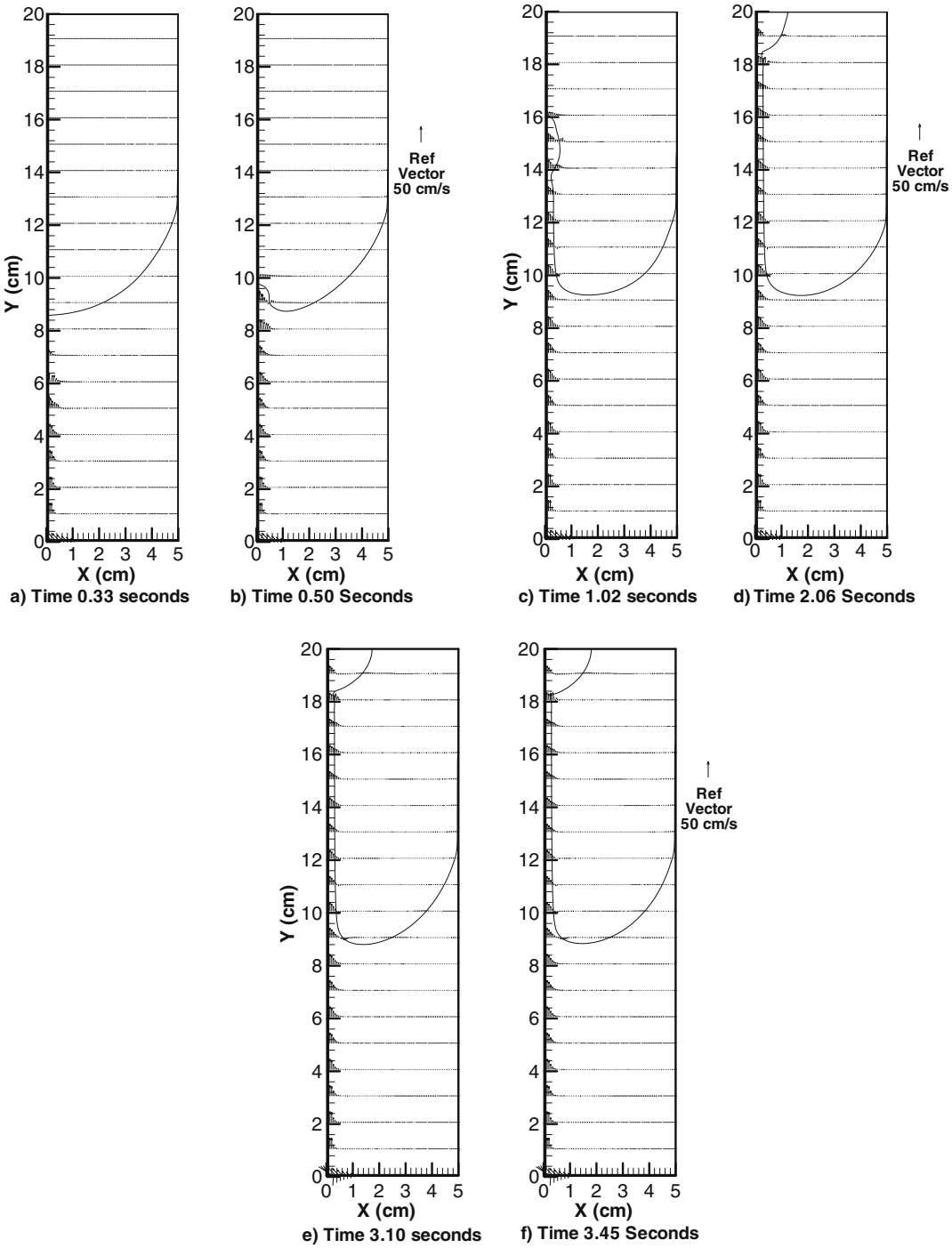

Fig. 4. Test 19, jet velocity 34 cm/s, fill height 8.9 cm at the centerline.

viscosity. Pope [35] using the experimental data of Hussien et al. [36] shows that turbulent viscosity is constant ±15% through the bulk of the jet although it does die down to 0 at the edge. Unfortunately Pope gives this constant in a non-dimensional form not readily available to use in our analysis. Schlichting [37] gives another formula for the average value of turbulent viscosity as a function of mean flow rate. This formula is

$$\mu_t = \rho A \sqrt{\frac{3K_a}{\pi}}, \tag{29}$$

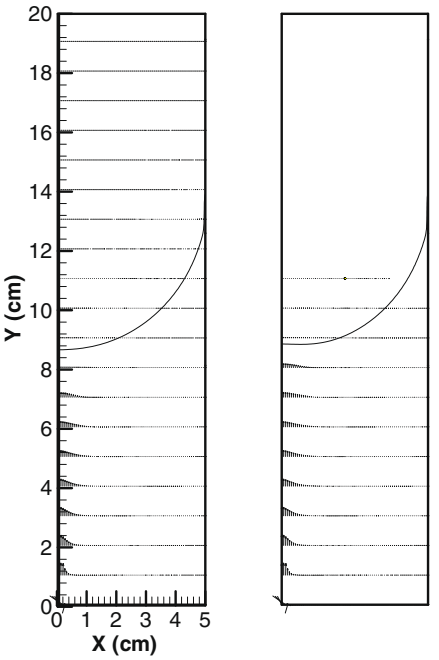

a)Time 0.68 seconds

where

$$K_a = 2\pi \int_0^{\infty} \bar{u}^2 r\, dr \tag{30}$$

and A is empirically determined to be 0.017. Using this formula $\mu_t = 0.158$ g cm/s when the velocity is 34 cm/s and $\mu_t = 0.232$ g cm/s when the velocity is 50 cm/s.

It is a fairly simple matter to introduce this as a new viscosity throughout the flow field. Although this is a pretty crude approximation its main effect is to suppress flows outside the main jet. It is believed that for the phenomena of geyser

Table 2
Geyser height comparison for laminar runs.

Test	Model ratio of geyser height to tank radius	Measured ratio of geyser height to tank radius
1	1.22	0.55
12	0.22	.36
15	0.1	.42
17	0.78	.34
50	0.1	.24
64	0.1	.10

height, which we are trying to investigate that major influence, is jet spreading which will still be accurately modeled by this approach. Flows at $Re = 450$ are omitted since they are already well modeled by the laminar test. Fig. 5 shows a representative runs. Unfortunately the fully turbulent model overcorrects resulting in lower predicted geyser heights than experimentally measured. Table 3 shows a numerical comparison between predicted and measured heights. Also included are the previous predictions of Schrader and Hochstein [29] (only available for a few runs).

4.6. Parametric variation of the turbulent viscosity

In an effort to improve the modeling of geyser height a parametric variation of the value of turbulent viscosity was conducted. Variation was focused on the 50 cm/s runs because these are the ones with the most deviation from measured values. The effort started by looking at test 14. Initially the turbulent viscosity was dropped to 0.14 g cm/s. The 0.14 g cm/s viscosity data over-predicted the geyser height, yielding a non-dimensional geyser height of 2.5 rather than the measured value of 2.16.

By looking at the results of the 0.232 g cm/s geyser height and 0.14 g cm/s a new value of 0.18 g cm/s was estimated. All 50 cm/s runs were modeled with this viscosity. Fig. 6 shows the results for test 52 that is the closest match to the experimental data. Table 4 shows a numerical comparison between predicted and measured heights.

Overall the 0.18 g cm/s viscosity data matches the experimental data reasonably well. The model still under predicts slightly most of the data but matches the test 52 data very closely.

4.7. Flow model in the turbulent regime

The full turbulence model under predicts geyser height for transitional flow. The agreement of the model was better than the previous model of Schrader and Hochstein [29] and converged for all runs instead of just a few. Adjustment of turbulent model coefficient can enable the model to match experimental geyser height but there is insufficient information on the flow field to determine the correct value. Geyser stability seems closely linked to the spread rate of the jet. Several other turbulence models were explored but not implemented. The work of Hochstein et al. [22] used a *k–epsilon* model with the Pope [38] correction for axial jets. However, the predictions of Hochstein et al. [22] do not seem any better than the ones we obtained with a much simpler model. Rubel [39] showed that the Pope correction factor produces poor results for the radial outward jet which is the other key feature of our simulation. Large Eddy models of turbulence were also considered, but the implementation of these would require construction of a full three-dimensional model of the flow field. The correct coefficients for the Large Eddy models of axial jets are still a matter of research [40]. Hence it was felt that the correct laminar–turbulent transition length is unlikely to be predicted by turbulence model. It is felt that the laminar–turbulent transition length determines spread of jet. So the Large Eddy model would have substantially increased the complexity of the code without much prospect of improved results.

5. Parametric studies

Once the code's performance against the experimental cases has been established, the code was used to understand the parameters and influences that lead to the geyser shapes observed. Several parameters which where not studied in the experiment where selected for further analysis (actually most of these parameters would be quite difficult to vary experimentally but can be changed easily by computer). Computer runs were made and the results analyzed. Findings are reported below.

5.1. Contact angle

The first parameter to be studied was the effect of changing wall contact angle. This value can be changed with a single input into the code. It is of interest because it varies greatly in the liquids used in spacecraft (water 60°, cryogens 0°). It also gives a range of free surface forces (90° no force, 0° maximum force.) This change enables us to study how changes in the equilibrium shape without the jet influence the final geyser shape.

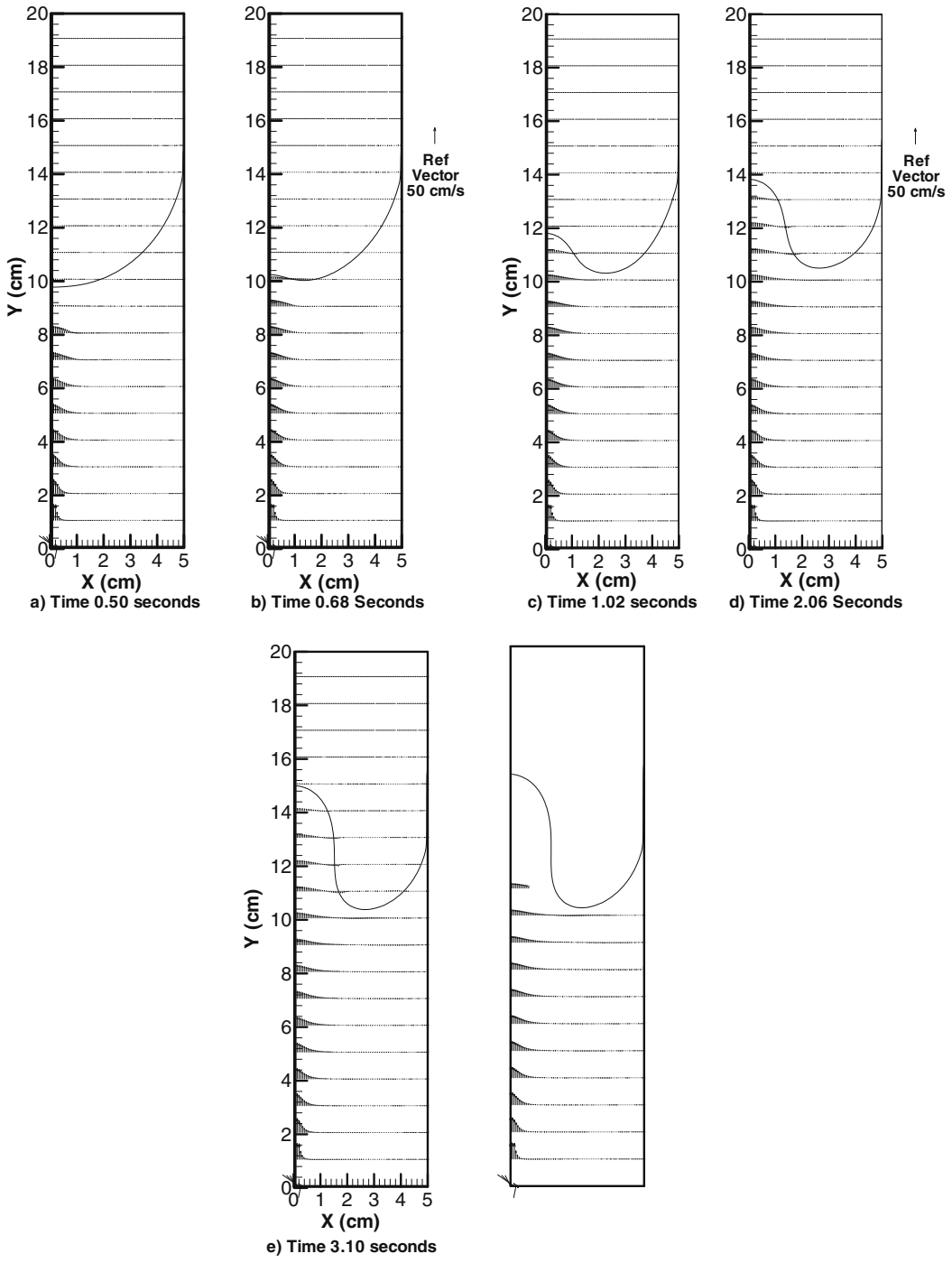

Free surface shapes are plotted in Fig. 7 for various contact angles for a jet of 17 cm/s at 3.10 s with a liquid fill height of 6.5 cm. The 30° contact angle acts to raise the free surface by only 0.02 cm over the 0° geyser height. The 60° contact angle raises slightly more about 0.12 cm from the 0° mark. The 90° contact angle increases the geyser height by 0.19.

Although the geyser heights increase they are not directly proportional to the change in equilibrium free energy. It can be shown that the equilibrium free surface radius of a tank with a finite contact angle is a spherical segment of a sphere of larger radius. Hence it should be the same as that of a larger tank with a smaller contact angle.

Table 3
Geyser height comparison for turbulence model.

Test	Model ratio of geyser height to tank radius	Prediction of Schrader	Measured ratio of geyser height to tank radius
13	0.36	0.36	.84
14	1.22	N/A	2.16
19	0.26	N/A	.52
24	0.82	N/A	1.45
51	0.26	N/A	.42
52	0.7	N/A	1.10
53	0.22	0.21	.30
57	0.46	0.45	.70
65	0.14	N/A	.20
66	0.26	N/A	.48

Table 4
Geyser height comparison with improved turbulence model.

Test	Model ratio of geyser height to tank radius	Prediction of Schrader	Measured ratio of geyser height to tank radius
14	1.66	N/A	2.16
24	1.2	N/A	1.45
52	1.06	N/A	1.10
57	0.58	0.45	.70
66	0.4	N/A	.48

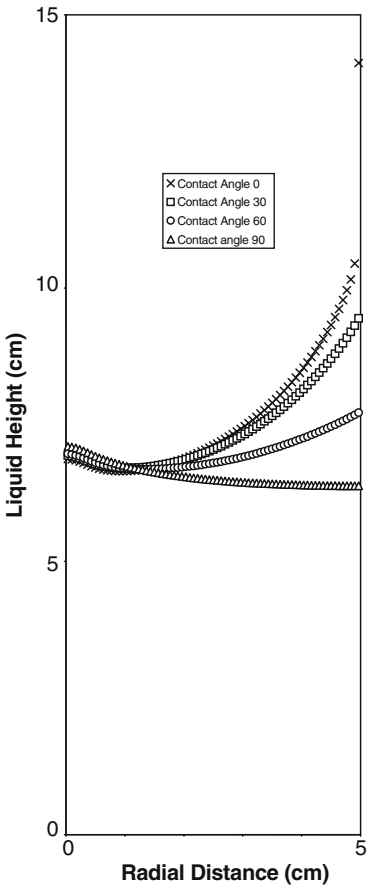

Fig. 7. Comparison of free surface shape as a function of contact angle.

Table 5
Volume comparisons.

Contact angle (°)	Total liquid volume (cm^3)	Geyser volume	Draw down volume
0	637.8	0.64	1.80
30	609.2	1.4	2.12
60	560.9	1.5	4.78
90	510.5	2.06	7.2

One factor that may reduce the geyser height with increasing contact angle is the change in liquid volume. In order to obtain the same fill height at the centerline and match the equilibrium free surface shape the liquid volume for the 30, 60, and 90 contact angles had to be reduced. Table 5 shows fluid volumes for each test. Since the total quantity of liquid is fixed, in order for the geyser to rise liquid in the outer regions of the tank must draw down. To estimate the shift in level from this effect the liquid interface shape was compared to the equilibrium free surface. Geyser volume was estimated by taking the volume of liquid above the equilibrium line in the center of the tank. Liquid draw down was estimated by the volume of gas below the equilibrium free surface. These two volumes are tabulated in Table 5.

In theory the two quantities should be exactly equal, in practice the liquid draw down is greater. Calculation of total volume based on free surface position shows some loss in total fluid volume as the calculation progresses. Evaluation of the total color function shows no change so the fluid must be lost in the spreading of the color function at the interface. Because the delta volumes at the interface are small volumes compared to the total volume they are much more influenced by this inaccuracy. A small volume loss of less than 1% can result in a tripling of the draw down volume. Once the liquid loss is removed from the draw down volume, the geyser volume and draw down volume are seen to match much more closely.

5.2. Tank wall

The results of the contact angle study suggested a significant influence of the wall on the final geyser height. To further study the influence of the wall, a tank with a radius of 10 cm was run with the same jet submergence as the 5 cm tank. The

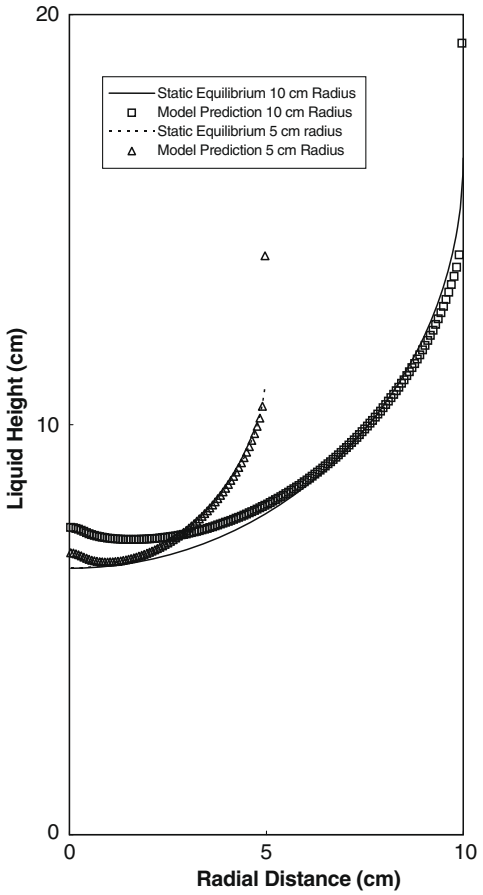

Fig. 8. Free surface shape comparison for tanks of different radius.

increased distance to the wall should reduce the influence of the wall and result in higher geyser height. Fig. 8 shows a comparison in free surface profiles at 3.1 s for a 17 cm/s jet at liquid height of 6.5 cm for a 0° 5 cm tank and a 0° 10 cm tank. The larger tank results in a geyser height increase of 0.61 cm. Some of this can be attributed to a decrease free surface energy. The surface pressure of a 10 cm radius bubble is only 4.48 dynes/cm^2 compared to 8.96 dynes/cm^2 for a 5 cm radius bubble, a decrease of 50%. Another part of this can be attributed to an increased geyser volume. In order to match the 6.5 cm at the centerline in the 10 cm tank liquid volume has increased to 3114 cm^3. This corresponds to a fill fraction of 49.6% rather than the 39% of the 5 cm tank. Geyser volume increases from 0.6 to 39.2 cm^3, while draw down volume becomes 41.9 cm^3 instead of 1.8 cm^3. Also of interest is the crossover point between the geyser and the draw down regions. This is at 7.5 cm, far beyond the 5 cm wall. This indicates that unconstrained the geyser influence extends beyond the 5 cm radius. Another comparison which is valuable is to compare to the 60° contact angle case. Analysis predicts the equilibrium shape for a 5 cm tank with a 60 contact angle and that of a 10 cm tank with a 0° contact angle to be identical. Fig. 9 shows a comparison of free surface shapes between the 5 cm and 60°, and the 60° equilibrium equivalent radius of 10 cm. Here one can see that the 60 contact angle on a 5 cm wall has acted to pin the free surface at a 0.2 cm lower level than would be reached by the 10 cm case at 5 cm. Also the contact angle formed by the 10 cm interface at the 5 cm mark is clearly less than 60°. Hence although the free surface equilibrium shapes are the same the jet deformed shapes are not.

To see the effect of the wall pinning without as much influence from changing free surface geometry a 10 cm radius tank with a 90° contact angle was also run. Fig. 10 shows a comparison between the 5 cm 90° run and 10 cm 90° run. Again the larger tank diameter produces an increase in geyser height. This cannot be attributed to the decrease in free surface energy since the 90 contact angle provides no pressure across the interface. Draw down level does not seem to be important either since both cases draw down level is about the same. However, it appears that the 5 cm wall prevents the jet from expanding as much as it would like.

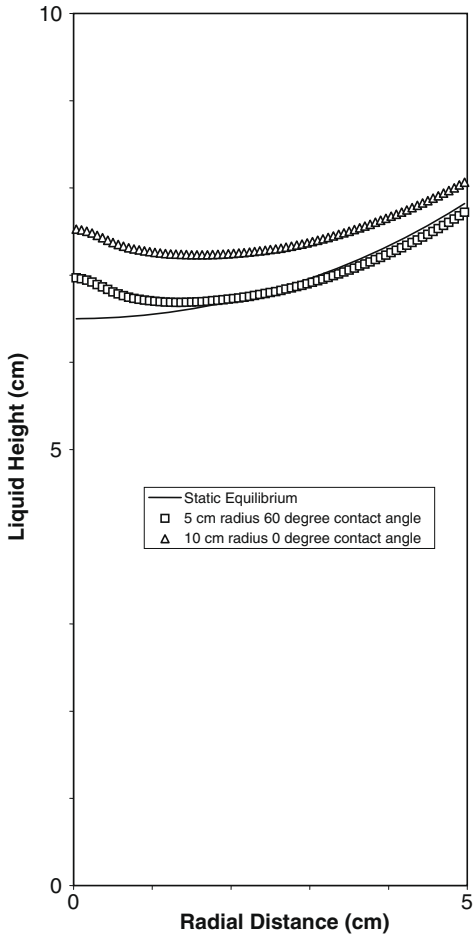

Fig. 9. Comparison of free surface shapes between a tank of 10 cm radius with 0° contact angle and a tank of 5 cm radius with a 60° contact angle (same ideal free surface shape).

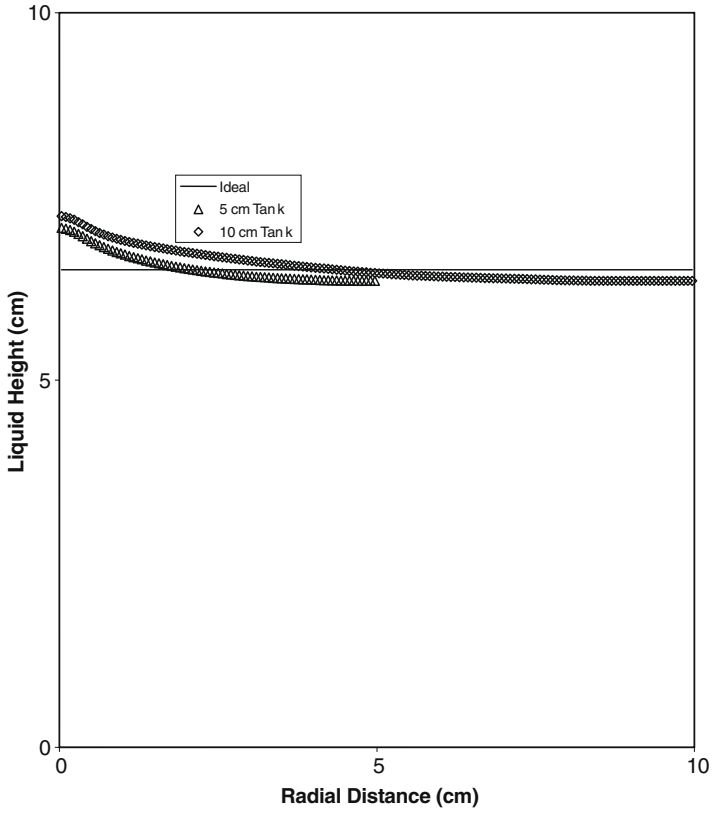

Fig. 10. Free surface shape comparison between 5 cm and 10 cm radius tanks with 90° contact angles.

5.3. Surface tension

In order to study a broad range of free surface shapes without changing the flow field significantly, it was decided to parametrically vary the surface tension. Physically this is a bit unrealistic since surface tension is a fixed function of the test fluids thermodynamics and cannot be arbitrarily selected. However, if one looks at the dimensionless quantities of Reynolds number and Weber number (which were shown in prior chapters to be the key dimensionless quantities governing geyser formation), Surface tension is the only parameter in the Weber number which can be changed without changing the Reynolds number as well. This makes the parametric investigation of surface tension a powerful tool for the investigation of the effect of the free surface on the geyser process while holding the bulk flow field constant. Table 6 lists surface tension, Weber number, geyser and draw down volumes.

Fig. 11 shows a comparison of free surface shapes for different values of surface tension after 3.1 s of flow. As expected unbounded geyser growth occurs at a Weber number of about 1 where the flow force just starts to exceed the surface tension forces. Fig. 12 shows axial velocity profiles for each of the runs at 6 cm from the tank bottom. They are almost indistinguishable indicating the validity of our assumption that the bulk flow is mostly unaffected by surface tension. Fig. 13 shows the radial velocity flows at 0.6 cm from the centerline (about the edge of the jet at a height of 6 cm from the bottom) here marked differences become apparent. The first is the shift in radial jet location caused by free surface motion. The second is that free surface deformation seems to broaden the radial outflow jet but reduce the peak magnitude. Table 7 shows the mass flow balances for each jet.

Table 6
Results for surface tension changes.

Surface tension (dynes/cm)	Weber number	Geyser height (cm)	Geyser volume (cm^3)	Draw down volume (cm^3)
5.6	1.96	16.7	15.1	17.1
11.2	0.98	8.90	18.0	17.2
16.8	0.65	7.19	4.43	5.96
22.4	0.49	6.88	0.64	1.80
44.8	0.25	6.79	2.81	3.7

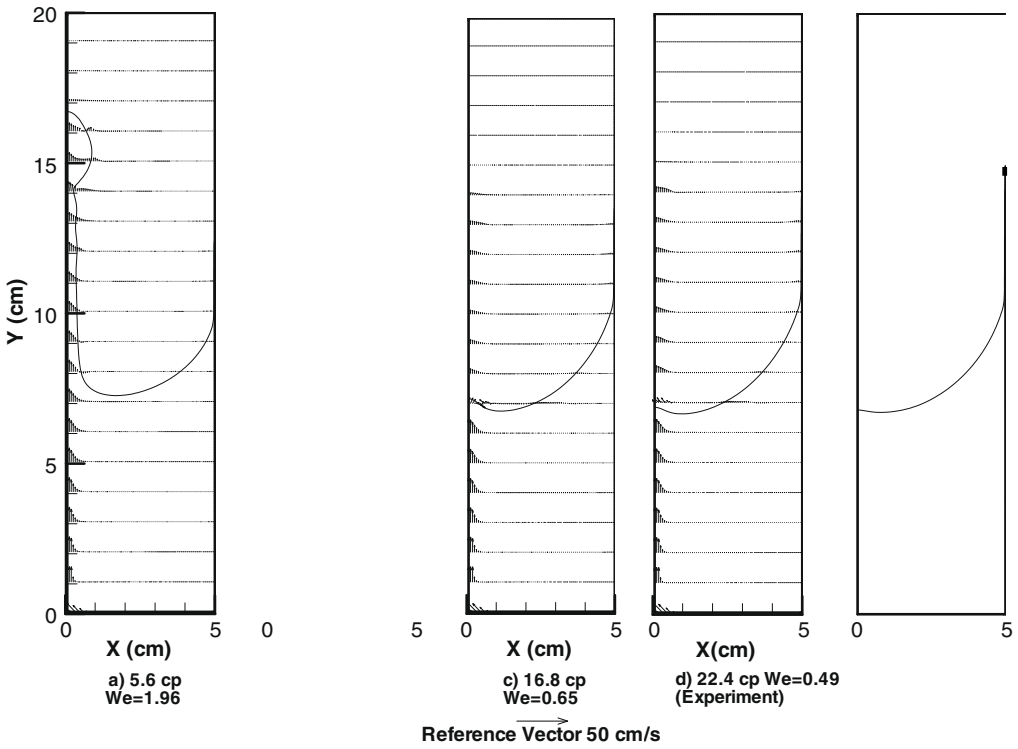

At the lowest surface tension the mass flow out of the jet region is much smaller than the mass entering supporting our finding of unstable jet growth. Looking at our three stable cases free surface deformation seems to broaden the radial outflow jet but reduce the peak magnitude.

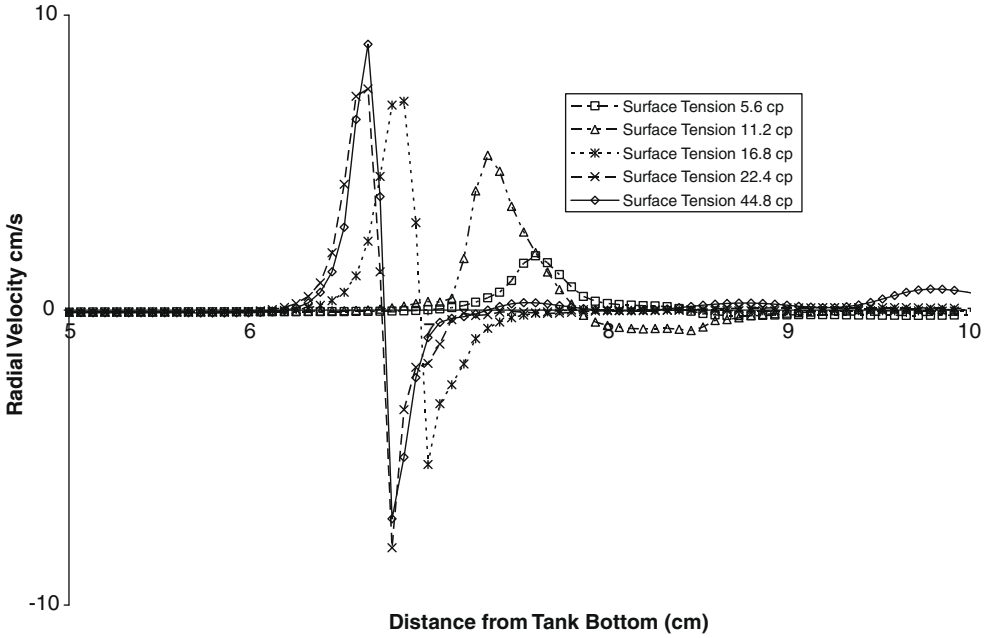

Fig. 13. Radial velocity at 0.6 cm from centerline.

Table 7
Mass balance for surface tension variation.

Surface tension	Mass flow in (axial flux at 6 cm from the bottom)	Mass flow out (radial flux at 0.6 cm from the centerline)
5.6	3.65	1.89
11.2	3.65	3.40
16.8	3.65	3.19
22.4	3.65	3.00
44.8	3.65	4.03

6. Summary

This paper documents the adaptation of the Jacqmin algorithm to the problem of restraint of liquid jets. Adaptations include formulation of an axisymmetric fourth order model, implementation of a symmetric boundary condition at the tank centerline, and enhancement of the wall wetting boundary condition to fourth order accurate. A simple velocity forcing function has been added to simulate the jet without violating continuity. Comparison to laminar drop tower tests has shown reasonable agreement between code predictions and measured geyser heights. A simple turbulence model has been shown to improve code agreement with flows in the turbulent transition region.

Model results were found to be in fair agreement with the experimental data of Aydelott [18]. Trends were similar but measured geyser heights were not matched. For low flow rates where laminarity could be assumed the model was found to under predict the experimental height. As the flow rate increased the model began to overpredict the geyser height, and under predict the jet spread rate. It is believed that turbulence was beginning to increase the jet spread rate as the flow rates increased into the turbulent onset rate. The importance of jet spreading on geyser stability is also apparent. Addition of a simple turbulent viscosity was able to improve the model prediction at the higher flow rates. The assumption of full turbulence everywhere did cause the model to once again under predict the geyser height. However, the underprediction of this model was less than prior modeling by Schrader and Hochstein [29], and this model could predict solutions for all cases whereas Schrader's model often failed to converge. Geyser height could be matched to the experiment by tuning the turbulent coefficient, but lack of velocity data in the Aydelott experiment makes it impossible to determine the correctness of the flow field created by this approach.

Parametric investigation produced several interesting finding. Investigation of the contact angle showed the expected trend of increasing contact angle increasing geyser height. Investigation of the tank radius showed some interesting effects and demonstrated the zone of free surface deformation is quite large. These finding may call into question the assumption of Aydelott [18] that a 5 cm radius tank is large enough that the wall has little effect on geyser height. Variation of the surface

tension with a laminar jet showed clearly the evolution of free surface shape with Weber number. Its predicted breakthrough is a Weber number of 1 as opposed to 1.5 found for the experimental results showing the influence that turbulent jet spreading has on decreasing geyser height.

Areas of future work should include the following: Improvement of the code so that a finer grid can be implemented in the jet region allowing a more detailed study of velocity profile. Using the information gained from the model to conduct a new drop tower campaign to further study the influence of tank diameter, jet diameter, and geyser growth rate. Consideration of a flight experiment to take the data beyond what is achievable in drop towers.

References

[1] M.D. Bentz et al., Tank pressure control experiment – a low-*g* mixing investigation, AIAA 90-2376.
[2] Michael D. Bentz, Tank pressure control in low gravity by jet mixing, NASA-CR-191012, March 1993.
[3] M.D. Bentz, R.H. Knoll, M. Hasan, C.S. Lin, Low-*g* fluid mixing – further results from the tank pressure control experiment, AIAA PAPER 93-2423, June 1993.
[4] Mohammad M. Hasan, Chin S. Lin, Richard H. Knoll, Michael D. Bentz, Tank pressure control experiment: thermal phenomena, NASA TP 3564, March 1996.
[5] Michael D. Bentz et al., Tank pressure control experiment – results of three space flights, AIAA Paper 97-2816, July 1997.
[6] D.J. Chato, T.A. Martin, Vented tank resupply experiment – flight test results, AIAA 97-2815, July 1997.
[7] D. Jacqmin, Calculation of two-phase Navier–Stokes flows using phase-field modeling, Journal of Computational Physics 155 (1999) 96–127.
[8] E.P. Symons, R.C. Nussle, K.L. Abdalla, Liquid inflow to initially empty, hemispherical ended cylinders during weightlessness, NASA TN D 4628, June 1968.
[9] Eugene P. Symons, Ralph C. Nussle, Observations of interface behavior during inflow to an elliptical ended cylinder in weightlessness, NASA TM X-1719, January 1969.
[10] Eugene P. Symons, Interface stability during liquid inflow to initially empty hemispherical ended cylinders in weightlessness, NASA TM X-2003, April 1970.
[11] Eugene P. Symons, John V. Staskus, Interface stability during liquid inflow to partially full, hemispherical ended cylinders in weightlessness, NASA TM X-2348, August 1971.
[12] Charles M. Spuckler, Liquid inflow to initially empty cylindrical tanks in low gravity, NASA TMX-2613, August 1972.
[13] John V. Staskus, Liquid inflow into a baffled cylindrical tank during weightlessness, NASA TM X-2598, August 1972.
[14] T.L. Labus, J.C. Aydelott, C.R. Andracchio, Effect of baffles on inflow patterns in spherical containers during weightlessness, NASA TMX-2670, November 1972.
[15] J.C. Aydelott, Axial jet mixing of ethanol in spherical containers during weightlessness, NASA TM X-3380, April 1976.
[16] J.C. Aydelott, Axial jet mixing of ethanol in cylindrical containers during weightlessness, NASA TP-1487, July 1979.
[17] J.C. Aydelott, Modeling of space vehicle propellant mixing, NASA TP-2107, January 1983.
[18] Thomas L. Labus, Liquid jet impingement normal to a disk in zero gravity, NASA TP 1017, August 1977.
[19] P. Concus, Capillary stability in an inverted rectangular tank, Advances in Astronautical Sciences 14 (1963) 21–37.
[20] P. Concus, Static menisci in a vertical right circular cylinder, Journal of Fluid Mechanics 34 (part 3) (1968) 481–495.
[21] R.E. Nickell, R.I. Tanner, B. Caswell, The solution of viscous incompressible jet and free surface flows using finite element methods, Journal of Fluid Mechanics 65 (Part 1) (1974) 189–206.
[22] J.I. Hochstein, P.M. Gerhart, J.C. Aydelott, Computational modeling of jet induced mixing of cryogenic propellants in low-*G*, AIAA 84-1344.
[23] J.I. Hochstein, Computational modeling of jet induced mixing in cryogenic propellant tanks in low-*G*, Ph.D. Thesis, The University of Akron, 1984.
[24] J.C. Aydelott et al., Numerical modeling of on-orbit propellant motion resulting from an impulsive acceleration, NASA TM-89873, 1987.
[25] J.J. Der, C.L. Stevens, Low-gravity bubble reorientation in liquid propellant tanks, AIAA 87-0622, January 1987.
[26] James Tegart, Three-dimensional fluid interfaces in cylindrical containers, AIAA 91-2174, June 1991.
[27] K.A. Brakke, "Surface evolver manual" minimal surface team of the geometry supercomputer. <geom.umn.edu>.
[28] J.U. Brackbill, D.B. Kothe, C. Zemach, A continuum method for modeling surface tension, Journal of Computational Physics 100 (2) (1992).
[29] G.B. Schrader, J.I. Hochstein, Modeling of jet-induced geyser formation in low-gravity, AIAA 93-0256, January 1993.
[30] J.D. Van der Waals, The thermodynamic theory of capillarity flow under the hypothesis of a continuous variation of density (Verhandel/Konink. Akad. Weten., 1893, vol. 1, English Translation), Journal of Statistical Physics 20.
[31] J.W. Cahn, J.E. Hillard, Free energy of nonuniform systems: III. Nucleation in a two-component incompressible fluid, Journal of Chemical Physics 31 (3) (1959).
[32] L. Collatz, The Numerical Treatment of Differential Equations, 3rd ed., Springer-Verlag, 1960. Translated by P.G. Williams.
[33] A. Viilu, An experimental determination of minimum Reynolds number for instability in a free jet, Journal of Applied Mechanics, ASME (1962).
[34] K.J. McNaughton, C.G. Sinclair, Submerged jets in short cylindrical flow vessels, Journal of Fluid Mechanics, ASME 25 (1966).
[35] S.B. Pope, Turbulent Flows, Cambridge University Press, 2000.
[36] H.J. Hussien, S.P. Capp, W.K. George, Velocity measurements in a high-Reynolds-number, momentum-conserving, axisymmetric, turbulent jet, Journal of Fluid Mechanics 258 (1994) 31–75.
[37] H. Schlichting, K. Gersten, Boundary-Layer Theory, eighth ed., Springer-Verlag, 2000.
[38] S.B. Pope, An explanation of the turbulent round jet/plane jet anomaly, AIAA Journal 16 (1978).
[39] A. Rubel, On the vortex stretching modification of the *k–e* turbulence model: radial jets, AIAA Journal 23 (7) (1985) 1129–1130.
[40] A.T. Webb, N.N. Mansour, Towards LES Models of Jets and Plumes, Center for Turbulence Research, Annual Research Briefs 2000, Stanford University, 2000.